Surface composition and ordering of binary nanoparticle mixtures in spherical confinement

Journal:	*Molecular Systems Design & Engineering*
Manuscript ID	ME-ART-12-2019-000185.R1
Article Type:	Paper
Date Submitted by the Author:	27-Feb-2020
Complete List of Authors:	Gartner, III, Thomas; University of Delaware, Chemical and Biomolecular Engineering Heil, Christian; University of Delaware, Chemical and Biomolecular Engineering Jayaraman, Arthi; University of Delaware, Chemical and Biomolecular Engineering; University of Delaware, Materials Science and Engineering

Design, System, Application Statement for:

Surface composition and ordering of binary nanoparticle mixtures in spherical confinement

Thomas E. Gartner III, Christian M. Heil, Arthi Jayaraman

Nanomaterials that exhibit structural color (color arising from periodic spatial variations in refractive index) are a promising platform for optical device applications due to their robust and tunable optical characteristics. There is a growing body of work leveraging nanoparticle assembly to fabricate optical nanomaterials with controlled structural color, yet a comprehensive understanding of the link between processing conditions, particle assembly/ordering, and color response is incomplete. In this work, we utilize molecular dynamics simulations of a binary mixture of synthetic melanin and silica nanoparticles in spherical confinement to mimic the emulsion assembly of optically-active spherical "supraballs". We investigate how design parameters such as particle chemistry, particle size, particle mixture composition, assembly timescale, and supraball size control the spatial distribution of nanoparticles on the supraball surface and within the supraball. These structural characteristics control the optical response of the material, with supraball surface composition correlating to color, and nanoparticle ordering correlating to the presence/absence of iridescence. Our results inform the design of structurally-colored nanomaterials by revealing the design and processing parameters required to form precise supraball architectures. Additionally, this work increases fundamental knowledge of nanoparticle assembly near curved surfaces which may provide insight into other processes including spray drying and porous materials fabrication.

Submitted to *Molecular Systems Design and Engineering*

Surface composition and ordering of binary nanoparticle mixtures in spherical confinement†

Thomas E. Gartner III[1,♦], Christian M. Heil[1,♦], Arthi Jayaraman[1,2,*]

[1]Department of Chemical and Biomolecular Engineering, 150 Academy St., University of Delaware, Newark, DE 19716

[2]Department of Materials Science and Engineering, 201 DuPont Hall, University of Delaware, Newark, DE 19716

♦Equal contributions

*Corresponding author arthij@udel.edu

†Electronic supplementary information (ESI) available.

Abstract:

We use coarse-grained Langevin dynamics simulations in shrinking spherical confinement to probe the fabrication of spherical "supraballs" via the emulsion assembly of binary nanoparticle mixtures. We examine a binary mixture of silica and synthetic melanin nanoparticles and discuss the structure and composition of the resulting supraballs particularly in the context of optical nanomaterials applications. Our results demonstrate how particle chemistry, particle size, particle mixture composition, assembly timescale, and supraball size cooperate/compete to control the spatial distribution of particles on the surface and within the supraball. We find strong enrichment of melanin particles at the supraball surface, with the degree of enrichment decreasing with increasing melanin/silica size ratio. We observe appreciable crystalline ordering only in systems where the particles are of similar size, and we note that particle size dispersity, finite assembly timescale, and curvature of the supraball surface all serve to suppress particle ordering. We also report routes toward some interesting hierarchical structures such as core-shell supraballs. These findings provide design rules for the development of optical materials for structural color applications, and they also increase our fundamental understanding of nanoparticle organization near curved surfaces and may find relevance for processes such as spray drying and porous materials fabrication.

Introduction:

Leveraging surfaces/interfaces to direct the assembly of nanoparticles is a long-standing technique to create functional nanomaterials for applications including optical and energy-producing devices, nanoporous materials, and drug delivery.[1-3] The presence of a surface or an interface can alter the particle-particle interactions[4] and can serve to nucleate/direct particle organization, allowing for the tunable assembly of nanoparticles to form nanocrystals, flat films and coatings, or 3-dimensional assemblies.[5-11] In particular, there is a growing body of work using emulsion droplets to create μm-scale spherical "supraparticles" or "supraballs" composed of assembled nm-scale nanoparticles.[7, 12, 13] These supraballs have attracted significant recent attention as optical materials[14-18] exhibiting structural color (color arising from periodic spatial variations in refractive index).[19] Structural colors are superior to absorption-based colors as they are robust to degradation and can be tuned by merely adjusting the spatial length-scale of the variation in refractive index. Thus, structurally-colored supraparticles are attractive materials to act as colorants/additives in technological display, sensing, or high-performance coating applications. However, many such materials are iridescent due to the high degree of nanoparticle ordering within the supraballs, somewhat limiting their applicability in wide-angle display and some sensing applications.[17]

Recently, a reverse emulsion assembly technique was used to create tunable structurally-colored materials from synthetic core-shell nanoparticles comprised of melanin core and silica outer shell.[17] Melanin is an attractive material for structural color and advanced coating applications due to its high refractive index, UV-resistance, and advantageous thermal and electrical conductivity properties.[20] These melanin-silica core-shell particles were initially suspended in the aqueous phase of a water-in-octanol emulsion.[17] Due to the solubility of water in octanol, the emulsion droplets decreased in size over time as the water diffused into the octanol

phase, eventually forming weakly-ordered spherical nanoparticle assemblies (supraballs). As a result, the supraballs exhibited non-iridescent colors, which were easily tunable through the thickness of the silica shell. This same process was also applied to mixtures of silica particles (SPs) and synthetic melanin particles (SMPs).[21] Interestingly, in a mixture of SPs and SMPs, SMPs were strongly enriched at the water-octanol interface, completely covering the surface of the supraball even when the overall mixture was SP-rich. Our coarse-grained (CG) Langevin dynamics simulations showed that this phenomenon was due to differing contact angles of the SPs and SMPs at the water-octanol interface.[21] The SMPs extended further into the octanol phase due to their slightly higher hydrophobicity than the SPs, and as the emulsion droplets shrank, the SMPs excluded the SPs from the interface and forced the SPs back into the interior of the emulsion droplet, creating an SMP-dominated surface layer. This approach presents an intriguing platform to potentially create complex hierarchical structures such as core-shell supraballs or micro/nanoporous assemblies. Thus, there is a need for design rules to better understand the structures formed in binary nanoparticle mixtures under shrinking spherical confinement and to map the phenomena that control the development of surface composition and ordering in these assemblies.

Existing work on the assembly of nanoparticles directed by a moving interface has mostly focused on drying flat films.[11, 22-37] Through simulations, theory, and experiments, it has been well established that in mixtures of small and large particles, depending on the particle size ratio, particle concentration, and evaporation speed, surface segregation can occur via a mechanism termed “auto-stratification”. Under certain conditions, either the smaller *or* the larger particles can localize at the drying interface and subsequently form a small- or large-particle enriched layer at the film surface due to the variation in diffusion rates between the two species and the interplay

between particle diffusion and interfacial motion.[38] Recent work has shown that this general idea holds under spherical confinement as well, exhibiting similar phenomenon in mixtures of small and large colloids in drying spherical water droplets supported on superhydrophobic surfaces.[39] However, only a handful of studies have explored the effect of varying particle chemistries, and in general, the processes of nanoparticle organization/ordering in spherical confinement is less widely understood.[13] Furthermore, while systems that exhibit auto-stratification are relevant to the present work due to the ready analogies between evaporative drying and the emulsion assembly process, the surface segregation observed in the emulsion assembly of SP-SMP mixtures[21] proceeds by a fundamentally different mechanism driven by the strong particle-interface interactions, rather than the diffusiophoresis phenomena implicated in the auto-stratification literature.[29, 40] As described in detail in Ref. [21], strong particle-interface interactions can result in this interface-driven surface segregation in regimes (i.e., moderate assembly timescales and particle size ratios) that would not necessarily produce auto-stratification.

In this work, we perform CG Langevin dynamics simulations of a binary mixture of melanin and silica nanoparticles in shrinking spherical confinement with strongly attractive particle-interface interactions. We explore a large parameter space of varying particle size, mixture composition, assembly time (i.e., interfacial velocity), and supraball size (i.e., interfacial curvature), to map how these parameters affect the particle assembly. In the context of optical applications, the structure and composition of the supraballs in the outermost layers are believed to dominate the optical properties,[18, 41] so we characterize the surface composition and near-surface structure of these materials under varying process conditions to develop design rules for binary particle emulsion assembly. We find, in accordance with our prior computational and experimental work,[21] that SMPs are strongly enriched at the supraball surface for moderate SMP/SP size ratios,

but as the size ratios increase, this enrichment is suppressed. Furthermore, we note a tunability in the assembled structure as supraball size changes, from core-shell supraballs in smaller droplets to bulk-like mixtures in large droplets. Appreciable ordering/crystallinity of the particles only occurs when all particles are close to the same size, and we also map the effects of particle size dispersity and interfacial curvature in suppressing crystallinity. Lastly, we present a detailed step-by-step view of the assembly process and describe how the surface composition and near-surface structure develops as the assembly proceeds. These results provide design rules to build precisely tunable supraparticle assemblies as well as give fundamental insight into the process of particle assembly and ordering in shrinking spherical confinement with strongly attractive particle-interface interactions. The results discussed herein also have potential relevance to other important industrial processes such as spray drying or other nanomaterials applications such as porous materials fabrication, drug delivery, etc.

Methods:

Model:

To model the formation of supraballs over experimentally-relevant time and length scales, we use a coarse-grained (CG) approach that was validated in our recent work through direct comparison with experiments.[21] In the CG model, the SMP and SP nanoparticles are modeled as spherical particles with average diameter D_{SMP} and D_{SP} respectively. We incorporate particle size dispersity by modelling each particle type as 11 discrete groups of differing diameters (D_i). We select the relative population in each group based on a Gaussian distribution, with standard deviation 6% of the average particle diameter. The largest/smallest particles in the size distribution are three standard deviations above/below the average particle diameter. To evaluate the impact of particle size dispersity on our results, we also run several monodisperse systems with all particles having

an identical diameter, and we clearly identify all monodisperse systems in the results section. We set the characteristic mass m = 1.0 based on the mass of a D_M = 220 nm SMP calculated using its volume and mass density, and we scale all other particle mases by $(D_i/2)^3$ as well as include the mass density difference between SP (~2.3 g/cm^3) and SMP (~1.3 g/cm^3).[21] The characteristic length σ is 1.0 nm for all systems. The particles interact through the colloid Lennard-Jones (cLJ) potential[42] with Hamaker constants ($A_{SMP\text{-}SMP}$ = 0.25 ε, $A_{SP\text{-}SP}$ = 0.25 ε, $A_{SMP\text{-}SP}$ = 0.175 ε) as defined in our previous work.[21] The cLJ potential possess a short range attraction with strength set by the Hamaker constant and a hard core repulsion for pairwise distances less than the diameter of the particle(s).[21] The characteristic energy ε is set to 1.0 k_bT so that the reduced temperature T^* = 1.0 represents room temperature (298 K).

To mimic the water-octanol interface, the particles interact with a spherical wall representing the interface through an attractive harmonic potential. This potential is similar to the fluid-fluid interface potential used in Ref. [11], but with a slightly modified form to allow for attractive particle-interface interactions; this potential models the change in interfacial energy when particles adsorb to a liquid-liquid interface based on Young's equation for surface tension.[5, 43]

$$U_{i,w}(r) = \begin{cases} \frac{\epsilon_{i,w}}{\left(\frac{D_i}{2} - r_0\right)^2}\left[(R-r)^2 - 2r_0(R-r) + r_0^2 - \left(\frac{D_i}{2} - r_0\right)^2\right], & r > R - \frac{D_i}{2} \\ 0, \quad otherwise \end{cases} \quad (1)$$

In Equation 1, r is the radial location of a particle (with the center of the emulsion droplet defined as the origin), R is the radius of the emulsion droplet, and r_0 defines the particle-interface contact angle via $\theta_i = \arccos(2r_0/D_i)$. The relative well depth of the particle-interface attraction retains the same ratio between SMP and SP (1:2) as our prior work[21] and are set at $\varepsilon_{i,w}$ = 500 ε and $\varepsilon_{i,w}$ = 1000 ε for the 220 nm SMP and 220 nm SP, respectively. The $\varepsilon_{i,w}$ scales proportionally to $(D_i/2)^2$ for

other sized particles.[3, 5] The location of the attractive harmonic potential minimum (given by $r = R - r_0$) is adjusted to account for the different contact angles for SMP ($\theta_{SMP} = 100°$) and SP ($\theta_{SP} = 80°$). The range of the potential is set to a distance of $D_i/2$ towards the interior of the emulsion droplet, so the particles only feel the potential as they begin to touch the interface.

Simulation Method:

Particles are initially randomly placed inside a spherical region of radius up to ~13 μm to achieve an initial particle occupied volume fraction $\eta = 0.03$ to match experimental conditions.[21] We investigate a range of final supraball radius (R_∞) from 0.5 μm – 5.0 μm, which we control by adjusting the total number of particles in the system, ranging from ~64 to ~159,000 particles depending on the particular mixture, bulk volume fraction of SMP particles ($\phi_{SMP,\,B}$), and desired R_∞. We define the mixture composition, $\phi_{SMP,\,B}$, as the ratio of volume occupied by SMPs to the total volume occupied by all particles in the system, so $0.0 \leq \phi_{SMP,\,B} \leq 1.0$ depending on the mixture composition. Most simulations have between ~20,000 and ~60,000 particles. We utilize implicit-solvent Langevin dynamics, implemented in the LAMMPS software package,[44] to mimic solvent effects on the motion of the colloidal particles as well as maintain system temperature. Our choice of an implicit-solvent approach significantly reduces the computational load relative to explicit-solvent simulations, allowing us to explore larger systems than would be possible with other approaches, at the cost of neglecting hydrodynamic interactions. We discuss our justification for our implicit solvent approach, as well as potential impacts from neglecting hydrodynamic effects in the Discussion section below.

We set the LAMMPS thermostat damping coefficient for 220 nm SMP particles to 148.7 τ with $\tau = 55$ μs. We then scale the damping coefficient for all other sized SMP/SP particles based on that particle's size and mass to ensure all particles experience the same effective implicit solvent

viscosity.[45] We calculate the mapping between reduced simulation time τ and real units by equating the diffusion coefficient of a 220 nm SMP particle in simulations (obtained by fitting the long-time behavior of the mean-squared displacement of a D_{SMP} = 220 nm, η = 0.03 system under standard periodic boundary conditions) to that obtained by the Stokes-Einstein relation for a 220 nm particle in water at ambient conditions. After a short energy minimization step to adjust any overlapping particles from the randomized initial configuration, we equilibrate the system with purely repulsive particle-wall interactions at T^* = 2.0 for 10^6 τ. The system is then progressively cooled to T^* = 1.0 over $1.5*10^4$ τ and equilibrated again for another 10^6 τ at T^* = 1.0 prior to shrinking the emulsion droplet.

To model the moving water-octanol interface during the emulsion process, we reduce the radius of the spherical confinement over the course of the simulation. Experimental work with polymer and nanoparticle emulsions suggests that the radius of shrinking emulsion droplets can be empirically described by Equation 2.[46-49]

$$R(t) = (R_o - R_\infty)\left(1 - \frac{t}{\tau_s}\right)^\alpha + R_\infty \quad (2)$$

where $R(t)$ is the radius of the emulsion droplet at time t, R_o is the initial emulsion droplet radius, R_∞ is the final supraball radius, τ_S is the emulsion droplet assembly time, and α is a 'curvature' parameter which influences the time dependence of the wall location, with α = 1.0 representing a constant linear change in droplet radius over time. Cabral and coworkers have found a range in α values from 0.5 to ~4 for polymer and nanoparticle systems depending on the solvent(s) and initial suspension concentration used.[46-49] The radius of the spherical confinement decreases (i.e., the interface moves) over a total simulation time τ_S to produce a desired Peclet number (*Pe*), which characterizes the relative rate of interfacial motion to particle diffusion (high *Pe* indicates fast interfacial motion and vanishing *Pe* indicates slow interfacial motion). For most simulations, we

linearly shrink the spherical wall (i.e., $\alpha = 1.0$) at a constant velocity of 309.6 nm/s to produce τ_S = 30 s (*Pe* ~ 1.0 for a 220 nm particle, see Table 1 below) or 3096 nm/s for τ_S = 3 s (*Pe* ~ 10 for a 220 nm particle) but also vary α for some tests to probe effect of non-linear interfacial motion (see *Parameters Varied*). We introduce the attractive interactions between particles and the interface when we begin the reduction in $R(t)$ to mimic experimental emulsion assembly. Additionally, an $\alpha > 1.0$ leads to very slow shrinking during initial stages of assembly which would be similar to allowing for particles to equilibrate onto the interface before significantly shrinking the droplet. The simulation proceeds with the emulsion droplet radius shrinking with a time step of 0.0025 τ if 220 nm SMP and 220 nm SP are used or 0.00125 τ for all other systems until the assembled supraball is formed near $\eta \sim 0.6$ (varies based on the particular mixture and particle sizes). Configurations are sampled for analysis every $2.5*10^3$ τ during the shrinking process for τ_S = 30 s or $2.5*10^2$ τ for τ_S = 3 s. In Table 1 we list the diffusion coefficients (D^*) and approximate *Pe* for the nanoparticles considered in this study.

Table 1: Diffusion coefficient (D^*) and Peclet number (*Pe*) data for $R_\infty \sim 3500$ nm

D_i(nm)	D^*_{SP} (nm²/τ)	D^*_{SMP} (nm²/τ)	Pe_{SP}		Pe_{SMP}	
			τ_S = 30 s	τ_S = 3 s	τ_S = 30 s	τ_S = 3 s
130	182 ± 3	195 ± 1	0.6	6.0	0.6	6.0
220	114 ± 1	121 ± 1	1.0	10.0	1.0	10.0
660	38[a]	40[a]	3.1	31.0	2.9	29.0

[a]Estimated using Stokes-Einstein relationship to scale D_i = 220 nm data

Analyses:

Peclet (*Pe*) numbers are calculated based on $Pe = \frac{(R_0 - R_\infty) * v}{D_i^*}$, where v is the interfacial velocity and D_i^* is the particle's diffusion coefficient. The diffusion coefficient is determined by single-component mean-squared displacement (MSD) simulations at η = 0.03 for the 130 nm and 220 nm

particles (see ESI Figure S1 for the MSD plots). The diffusion coefficient for the 660 nm particles cannot be determined from MSD simulations at $\eta = 0.03$ because over the course of the simulation, the 660 nm particles aggregate due to the strong attractive interactions at large particle size (the well depth of the colloid Lennard-Jones (cLJ) potential scales with particle size). As such, the diffusion coefficient for the 660 nm particles is determined using an extrapolation from the respective 220 nm particle based on the Stokes-Einstein diffusion equation. We confirm the applicability of the Stokes-Einstein equation because the 130 nm and 220 nm particles (SMP and SP) match the scaling relation within ~5%.

To quantify the volume fraction of SMP particles on the surface of the supraball compared to all surface particles ($\phi_{SMP,\,S}$), we use a Voronoi decomposition-[50]based method to identify particles on the surface of the supraball. We first define the analytical supraball radius $R_a(t)$ to be the radial location of the particle farthest from the supraball center. Particles are defined to be "on the surface" if at least one of their Voronoi vertices is located at a radial distance greater than $R_a(t)$. This calculation is performed for all η, where we define η as the occupied volume of all particles divided by the emulsion droplet volume. We calculate the emulsion droplet volume for each configuration by applying a convex hull[51] analysis to a set of points defined by the outermost surface(s) of the particles (to correctly account for the particles' pervaded volume). To determine the volume fraction of SMP particles in the interior of the supraball compared to all internal particles ($\phi_{SMP,\,I}$), we define the supraball interior to be all particles with radial location $r < 0.75*R_a(t)$.

To characterize supraball ordering, we identify crystalline domains by calculating a bond-orientational order parameter q_{6m} originally defined by Steinhardt et al.[52] where "bonds" are defined based on particle pairs within a distance cut off of $1.4 * \frac{(D_i + D_j)}{2}$. Particles are identified as

'crystalline' (i.e., highly ordered) if a particle has 7 or more bonds with each bond having d_6(i,j) > 0.6, with d_6(i,j) given by[53]

$$d_6(i,j) = \frac{\sum_{m=-6}^{+6} q_{6m}(i) q_{6m}^*(j)}{\left(\sum_{m=-6}^{+6} |q_{6m}(i)|^2\right)^{1/2} \left(\sum_{m=-6}^{+6} |q_{6m}(j)|^2\right)^{1/2}} \quad (3)$$

where *i* represents the particle being considered and *j* represents its *j*th neighbor. We then assign particle pairs to a single crystalline domain if they are both highly ordered and have a d_6(i,j) > 0.8. Because our system includes particle size dispersity, we utilize a d_6(i,j) cut off of 0.8 instead of 0.9 as used by de Nijs et al.[53] Slightly reducing the cut off improves the identification/mapping of discrete domains without affecting overall trends in the number fraction of particles that participate in a crystalline-like domain (f_c). To identify crystalline ordering as a function of supraball layer, we determine the particles that are crystalline, use the previously described Voronoi decomposition approach to identify surface particles, and calculate the fraction of surface particles that are also crystalline. We then discard all of the particles identified as being on the surface and repeat this process to identify those in the supraball's second layer, etc.

We characterize particle jamming at the water-octanol interface by tracking the average magnitude of particle displacement on the emulsion droplet surface over a defined time period $\Delta t = 2500\ \tau$ throughout the assembly. We also deconstruct the total displacement of particles over Δt into "radial" and "surface tangent" components. For each particle on the emulsion surface, we denote its position at t and $t + \Delta t$ as $\vec{r}_1$ and $\vec{r}_2$, respectively. Then, we determine the projection of $\vec{r}_2$ onto $\vec{r}_1$ as $\vec{r}_{2,Project} = \frac{\vec{r}_1 \cdot \vec{r}_2}{\|\vec{r}_1\|^2}\vec{r}_1$. The radial component of the particle displacement is then $\vec{r}_1 - \vec{r}_{2,Project}$, and the surface tangent component can be found using the Pythagorean theorem since the total, radial, and surface tangent displacement vectors must form a right triangle.

In all plots and tables, error bars shown are the standard deviation from three independent replicates (different particle initial configurations and velocities). Three replicates are chosen because the observed variability between trials is small, indicating that final supraball surface composition is not overly sensitive to the initial state for the parameter space explored herein. We prepare simulation snapshots using the Visual Molecular Dynamics software.[54]

Parameters Varied:

We explore a range of design parameters including particle chemistry, particle size, $\phi_{SMP,\,B}$, τ_S, R_∞, and α. We investigate both single-component SMP supraballs and two-component SMP/SP mixtures. To determine particle size effects, we consider 130 nm, 220 nm, and 660 nm particles with the SP particle either the same size or smaller than the SMP particle because our previous work demonstrated that only systems with smaller SP particles resulted in supraball surfaces with $\phi_{SMP,\,S} < 1.0$.[21] We choose the particle sizes such that the size ratios are 1.0 (220 nm + 220 nm), ~1.7 (130 nm + 220 nm), 3.0 (220 nm + 660 nm), and ~5.1 (130 nm + 660 nm). To determine the impact of particle size dispersity, we consider both monodisperse and polydisperse systems. To investigate the impact of mixture composition we use $\phi_{SMP,\,B}$ = 0.1, 0.2, 0.5, 0.8, 0.9, and 1.0. To understand the impact of interfacial velocity, we explore τ_S of 30 s and 3 s. We investigate a span of R_∞ from 0.5 μm – 5.0 μm. Finally, we analyze the impact of α by considering three values: 0.5, 1.0, and 2.0.

Results:

As discussed in our prior computational and experimental work,[21] we observe several key steps in the assembly process as illustrated from left to right in Figure 1. During the early stages of the assembly, the particles are homogenously distributed throughout the emulsion droplet volume at low η (leftmost snapshot). As $R(t)$ decreases, particles diffuse and adsorb to the water-octanol

interface due to the strongly favorable particle-interface interactions (2nd image). Particles continue to adsorb to the interface until they form a jammed surface-adsorbed layer (the jamming transition of the surface-adsorbed particles is quantified in ESI Figure S2) at the water-octanol interface with total surface area coverage ~0.84. At this state the majority of particles are localized at the interface while a few remaining particles diffuse freely within the bulk of the emulsion droplet (3rd image). As $R(t)$ continues to decrease, particles are forced to desorb from the liquid-liquid interface due to the decreasing surface area of the emulsion droplet and increasing curvature of the spherical confinement; during this stage the particle concentration within the interior of the droplet progressively increases (4th image). Finally, at $t = \tau_S$, the particles form the assembled supraball (rightmost image). The final surface and interior structure and composition of the supraball for a given binary particle mixture is a result of the interplay between these various processes, which we explore in detail in this work.

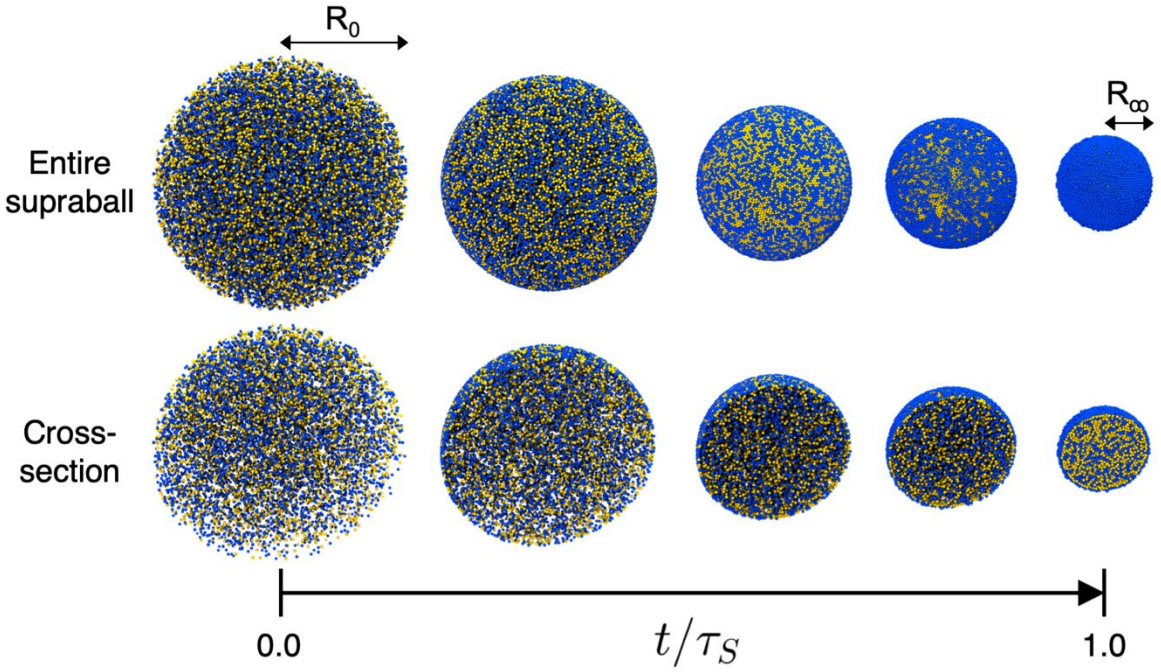

Figure 1: *Simulation snapshots illustrating key stages of the emulsion assembly for a $D_{SP} = D_{SMP} = 220$ nm, $\phi_{SMP,\,B} = 0.5$ mixture. SPs are rendered in yellow, and SMPs are rendered in blue. The*

upper row shows the entire emulsion droplet geometry, and the lower row shows a cross-section of the emulsion droplet. Snapshots are ordered chronologically from the initial configuration at $t/\tau_S = 0.0$ (left) to the assembled supraball at $t/\tau_S = 1.0$ (right).

We first discuss the impact of interfacial curvature of the emulsion droplet/supraball (i.e., R_∞) on the structure and composition at the surface and in the interior of the supraball. As described in the methods section, we quantify the composition of the surface of the supraball ($\phi_{SMP,\,S}$) and within the supraball interior ($\phi_{SMP,\,I}$) and characterize the degree of particle ordering by calculating the overall number fraction of particles that participate in a crystalline-like domain (f_c). Within the context of optical materials, $\phi_{SMP,\,S}$ should largely control the color of the resulting supraballs,[21, 55] while f_c should correlate with the presence/absence of iridescence.[18, 56] $\phi_{SMP,\,B}$ differs from $\phi_{SMP,\,I}$ because $\phi_{SMP,\,B}$ incorporates all SMP particles regardless of their spatial position while $\phi_{SMP,\,I}$ only includes SMPs defined to be localized in the supraball interior (see Methods section for $\phi_{SMP,\,I}$ definition). In Figure 2a we plot $\phi_{SMP,\,S}$ and $\phi_{SMP,\,I}$ as a function of R_∞ for three representative SMP/SP mixtures: 1) particle diameters $D_{SP} = D_{SMP} = 220$ nm, mixture composition $\phi_{SMP,\,B} = 0.5$, 2) $D_{SP} = D_{SMP} = 220$ nm, $\phi_{SMP,\,B} = 0.1$, 3) $D_{SP} = 130$ nm, $D_{SMP} = 660$ nm, $\phi_{SMP,\,B} = 0.5$. All systems in Figure 2 assemble over a time scale $\tau_S = 30$ s, corresponding to a *Pe* ranging from 0.6 to 3.1 depending on particle size. Thus, for the systems in Figure 2, the particle diffusion rate is comparable to the rate of interfacial motion. We present in detail the potential impacts of neglecting hydrodynamic interactions in the Discussion section below; briefly, we expect hydrodynamic interactions to become increasingly crucial as *Pe* increases. Given that the results reported in this section are at relatively low *Pe*, we argue that our results may be *quantitively* impacted by neglecting hydrodynamics, but we expect the *qualitative* trends to not be affected. We observe that the surface and interior composition of the supraballs at a given $\phi_{SMP,\,B}$ can be tuned by adjusting R_∞. Such tunability could be achieved experimentally by adjusting the

parameters of the vortex mixing or the flow rates in a microfluidic-type device to control the initial size of the emulsion droplets.[46] At small R_∞, the vast majority of the SMP particles are located on the surface (i.e., high $\phi_{SMP,\,S}$) and are absent in the supraball interior (i.e., low $\phi_{SMP,\,I}$); effectively the supraball exhibits a core-shell structure (ESI Figure S3). As R_∞ increases, $\phi_{SMP,\,I}$ approaches $\phi_{SMP,\,B}$ for all three systems examined. In Figure 2b, we observe crystalline ordering (i.e., a non-zero f_c) only for systems where the SPs and SMPs are the same size. Furthermore, crystallinity is suppressed at low R_∞, due to the increased frustration of crystalline packing introduced by the surface curvature.[13] The transition from low to high f_c occurs when the R_∞ is approximately 20 times the nanoparticle size; above this critical R_∞, f_c is only weakly dependent on R_∞. For particles participating in a crystal domain, we calculate a global bond-orientational order parameter $Q_6 \approx 0.57$, indicating that most of the crystalline particles are participating in FCC-like ordering.[52] That finding is in agreement with prior experimental and computational work on the emulsion assembly of similar systems that found FCC particle ordering in supraballs/supraparticles formed through emulsion assembly or simulation methods mimicking emulsion assembly.[57-59]

To aid in the interpretation of the quantitative data in Figure 2a-b, in Figure 2c-e we show simulation snapshots of the assembled supraballs from these three mixtures for $R_\infty = 3.5$ μm (simulation snapshots for all systems in Figure 2 are shown in ESI Figure S3). The left and center images in Figure 2c-e show the SPs rendered in yellow and the SMPs rendered in blue, and the surface segregation of SMP particles is easily visible in 2c-d. The rightmost image shows particles colored by crystalline domain; this snapshot illustrates that most of the highly-ordered domains exist near the supraball surface, which we quantify in more detail below.

After examining the above trends, we choose to perform all subsequent tests at $R_\infty = 3.5$ μm as this choice represents a sufficiently large final radius to be representative of large supraballs,

while significantly reducing the computational resources required relative to the R_∞ = 5.0 μm systems. We generate the data in Figure 2 using an interface that moves at a constant rate (curvature parameter α = 1.0 in methods section Equation 2), but also tested non-linear changes in $R(t)$ (α = 0.5 and 2.0), which showed no effect on the trends in $\phi_{SMP,\,S}$, $\phi_{SMP,\,I}$ and f_c (ESI Figure S4). Thus, we select α = 1.0 for the rest of this study.

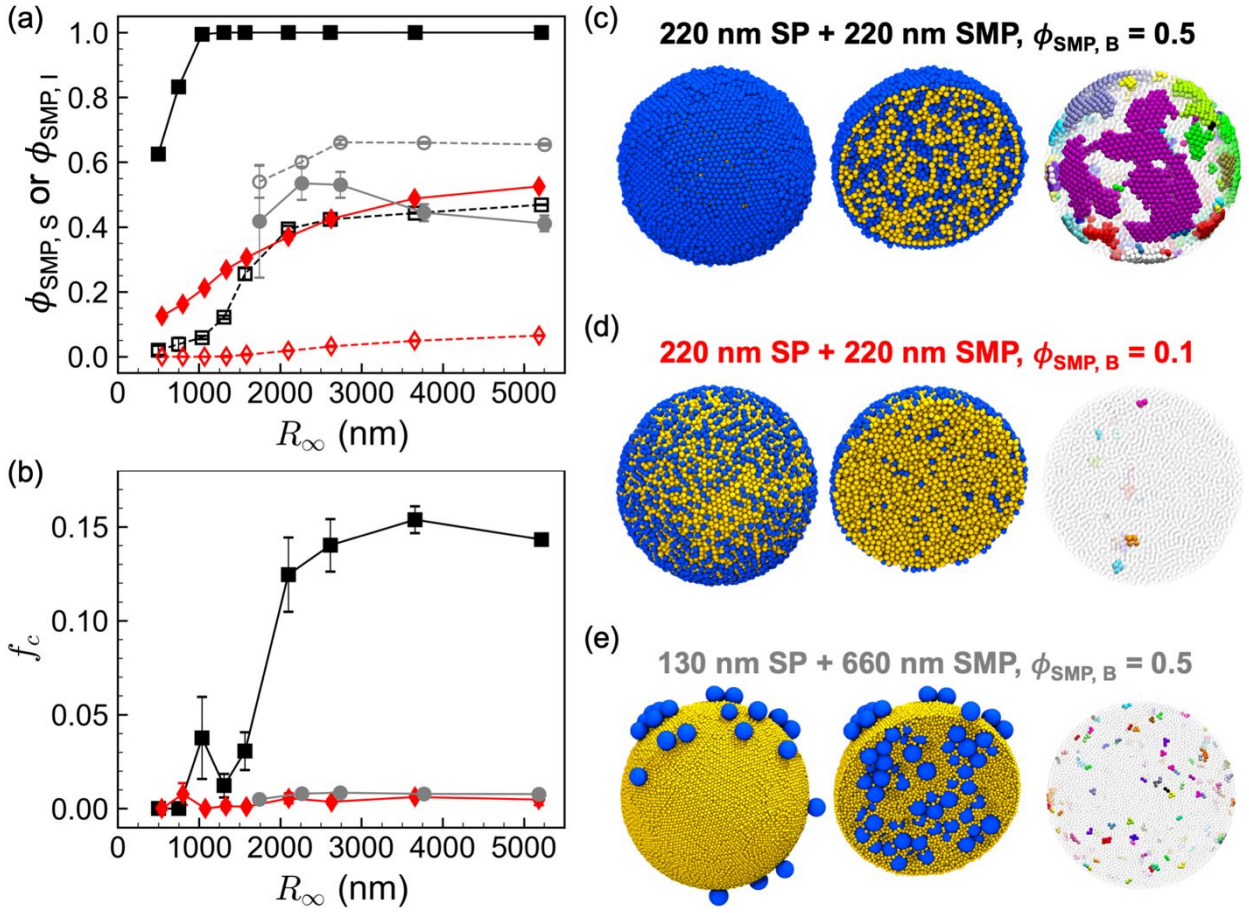

***Figure 2**: Impact of altering R_∞ on (a) $\phi_{SMP,\,S}$ (solid symbols and solid lines) and $\phi_{SMP,\,I}$ (open symbols and dashed lines) and (b) f_c. Black squares and the simulation snapshots in (c) are a D_{SP} = D_{SMP} = 220 nm, $\phi_{SMP,\,B}$ = 0.5 mixture, red diamonds and the simulation snapshots in (d) are a D_{SP} = D_{SMP} = 220 nm, $\phi_{SMP,\,B}$ = 0.1 mixture, and grey circles and the simulation snapshots in (e) are a D_{SP} = 130 nm, D_{SMP} = 660 nm, $\phi_{SMP,\,B}$ = 0.5 mixture. Panels (c-e) show simulation snapshots of the full supraball at R_∞ = 3.5 μm on the left, supraball cross section in the middle, and particles colored by crystalline domain on the right (particles not participating in an ordered domain are rendered in transparent grey). For all cases, τ_S = 30 s.*

Next, we explore how varying particle size, mixture composition, and assembly timescale affect the supraball characteristics. In Figure 3 we plot the impact of mixture composition ($\phi_{SMP,B}$) SMP/SP size ratio (D_{SMP}/D_{SP}) and time scale of assembly (τ_S) on supraball composition and f_c. When D_{SMP}/D_{SP} is small, $\phi_{SMP,S}$ is greater than $\phi_{SMP,B}$ (Figure 3a), indicating an enrichment of SMP particles on the supraball surface as seen in our previous work.[21] However, the degree of SMP enrichment at the surface decreases as D_{SMP}/D_{SP} increases; for D_{SMP}/D_{SP} = 5.1 (D_{SP} = 130 nm, D_{SMP} = 660 nm), $\phi_{SMP,S}$ approaches $\phi_{SMP,B}$. We attribute this behavior to differences in particle diffusion rates as D_{SMP}/D_{SP} increases (Table 1). The larger SMPs' lower diffusion rate results in an SP-rich interface during the early stages of the assembly, as the smaller SPs can diffuse and adsorb to the interface more quickly. Thus, fewer SMPs are located at the interface when the interfacial layer reaches the jammed state, resulting in a decreased $\phi_{SMP,S}$ in the final supraball. For small D_{SMP}/D_{SP}, decreasing τ_S results in a reduction in $\phi_{SMP,S}$; however, for D_{SMP}/D_{SP} = 5.1, the smaller τ_S increases $\phi_{SMP,S}$. We propose that this reversal is a result of the higher *Pe* at low τ_S (Table 1). As *Pe* increases, the effect of the different diffusion rates between small and large particles becomes less important, so more SMPs are incorporated into the water-octanol interface, increasing $\phi_{SMP,S}$. We anticipate that the impact of τ_S will become increasingly significant as D_{SMP}/D_{SP} increases beyond 5.1, as seen in thin-film evaporative assembly work.[38] While $\phi_{SMP,S}$ is strongly impacted by changing $\phi_{SMP,B}$, Figure 3b shows that $\phi_{SMP,I} \approx \phi_{SMP,B}$ for all mixtures, due to R_∞ = 3.5 μm being large enough to accommodate the SMP enrichment at the supraball surface without significantly changing the interior composition.

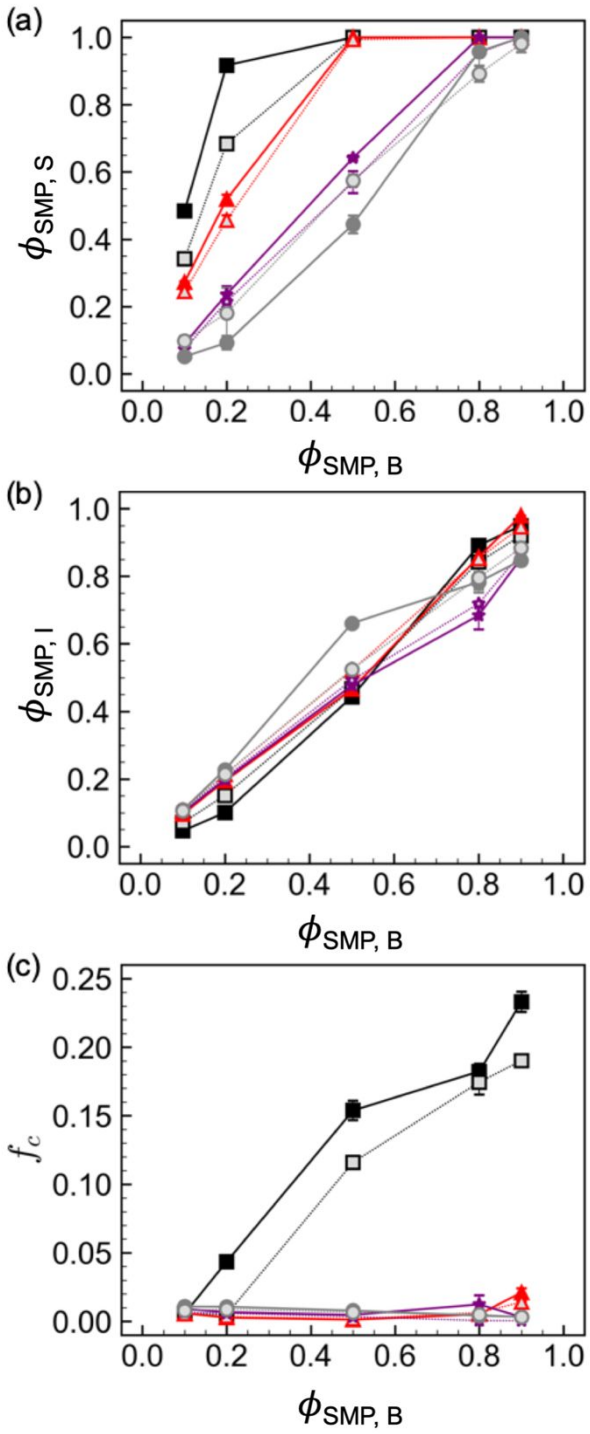

Figure 3: *Impact of altering particle mixture composition, $\phi_{SMP,\,B}$, on a) supraball surface composition, $\phi_{SMP,\,S}$, b) supraball interior composition, $\phi_{SMP,\,I}$, and c) fraction of crystallinity, f_c. Black squares are D_{SP} = D_{SMP} = 220 nm (SMP/SP size ratio =1.0), red triangles are D_{SP} =130 nm, D_{SMP} = 220 nm (SMP/SP size ratio =1.7), purple stars are D_{SP} =220 nm, D_{SMP} = 660 nm (SMP/SP size ratio =3.0), and grey circles are D_{SP} =130 nm, D_{SMP} = 660 nm (SMP/SP size ratio*

=5.1). Dark filled symbols and solid lines are τ_S = 30 s and light filled symbols and dotted lines are τ_S = 3 s. All results are for R_∞ = 3.5 μm and α = 1.0.

In Figure 3c we show the f_c as a function of D_{SMP}/D_{SP}, τ_S, and $\phi_{SMP,\,B}$. We find near-zero f_c when D_{SMP}/D_{SP} is greater than 1.0 for any condition. This result is due to the asymmetric particle diameters frustrating the formation of crystalline domains, in agreement with experimental results that observed disordered supraballs at a D_{SMP}/D_{SP} as small as 1.25 and computational results that found that ordering significantly decreased as particle size asymmetry increased.[18, 60] For the symmetric particle diameter case, Figure 3c illustrates that f_c increases monotonically with increasing $\phi_{SMP,\,B}$. We can explain this result by noting that at the finite assembly timescales studied herein, highly-ordered domains largely only occur on the supraball surface and within the outermost 2-3 layers (Figure 2 snapshots). At low $\phi_{SMP,\,B}$, on the supraball surface there is insufficient SMP (low $\phi_{SMP,\,S}$) to form ordered domains because SMPs are relatively dispersed across the surface, and the SPs have a lower contact angle than SMPs, preventing the formation of inter-particle type crystalline domains. As $\phi_{SMP,\,B}$ increases, the number of SMPs at/near the surface increases, enabling partial ordering on the supraball surface. Finally, at high $\phi_{SMP,\,B}$, the entire supraball surface becomes completely covered in SMP, and the higher $\phi_{SMP,\,B}$ results in crystallinity expanding into the first and second layers below the supraball surface. Decreasing τ_S to τ_S = 3 s results in a slight reduction in f_c, but all other trends remain the same. We note that significant changes in assembly mechanisms and or quantitative/qualitative results may be observed if τ_S was reduced even further than 3 s, as hydrodynamic interactions and/or auto-stratification phenomena become increasingly important at high *Pe* (low τ_S). Other simulation work found that changing the particle bulk volume fraction had no effect on ordering; however, that work did not include difference in particle contact angle for the varying particle types.[60] Thus,

we show that accounting for realistic differences in particle-interface contact angle not only is important in controlling supraball surface composition[21] but also in ordering/crystallinity.

In the previous figures, we discuss the final supraball structure and composition, but it is also instructive to examine how they develop temporally during the assembly process. In Figure 4 we show $\phi_{SMP,\,S}$, f_c, and number of particles on the surface of the emulsion droplet (N_S) as a function of time during the assembly (t/τ_S) for four representative systems: polydisperse and perfectly monodisperse pure-SMP ($\phi_{SMP,\,B} = 1.0$) and SMP-SP mixtures ($\phi_{SMP,\,B} = 0.8$) at $\tau_S = 30$s. These systems allow us to separately examine the impact of chemical heterogeneity (pure SMP vs. SMP-SP mixture) and physical heterogeneity (particle size dispersity) in particles on the development of supraball structure. These key observations labeled with numbers are shown in Figure 4: During the initial period of assembly, the SMP and SP particles diffuse and adsorb to the interface, indicated by an increasing N_S (marked as "1") until it reaches a plateau. As the emulsion droplet shrinks (i.e., decreasing interfacial area), a jamming transition[61] occurs (marked as "2"). We locate the jamming transition by tracking the magnitude of displacement of surface-adsorbed particles over time; at the jamming transition the surface tangent component of particle displacement drops to zero, see ESI Figure S2. After the formation of the jammed surface layer, particles start to be forced away from the interface (3) and into the interior of the droplet, illustrated by a decrease in N_S. At this point, f_c (and $\phi_{SMP,\,S}$, in the case of the binary mixtures) begins to increase. For the systems with particle size dispersity, we observe a structural rearrangement resulting in a small hump in f_c (4) as the emulsion droplet continues to shrink; interestingly, this rearrangement is absent in perfectly monodisperse systems. We believe that this rearrangement is caused by larger SMP particles forcing smaller SMP particles away from the interface because the particle-interface adsorption energy scales with particle radius squared,[5] so the larger SMP

particles are more strongly bound to the interface than the smaller ones. During this stage, f_c increases while N_S continues to decrease, indicating a preference for non-crystalline particles to be removed from the interface (5). Eventually, the droplet curvature becomes significant enough to frustrate particle crystallinity on the surface, as illustrated with the peak in f_c at (6), after which f_c decreases for all systems. However, as the droplet approaches the assembled state near t/τ_S, the monodisperse systems experience an uptick in f_c (7), whereas this behavior is not apparent in systems with particle size dispersity. The final uptick in f_c for the monodisperse systems is a result of monodisperse particles more easily organizing into ordered structures, resulting in the propagation of crystallinity deeper into the final supraball and a higher f_c (discussed in more detail in Figure 5 below). Decreasing τ_S from 30 s to 3 s has a small impact on the specific N_S, $\phi_{SMP,\,S}$, and f_c values for a given system as well as the relative temporal locations of the steps highlighted, but the key observations and the assembly pathway remain the same for the assembly timescales studied herein (ESI Figure S5). Thus, depending on the particle size(s), mixture composition, and the presence/absence of particle size dispersity, the interplay between these 7 key stages of assembly control the final composition and structure observed in the assembled supraballs.

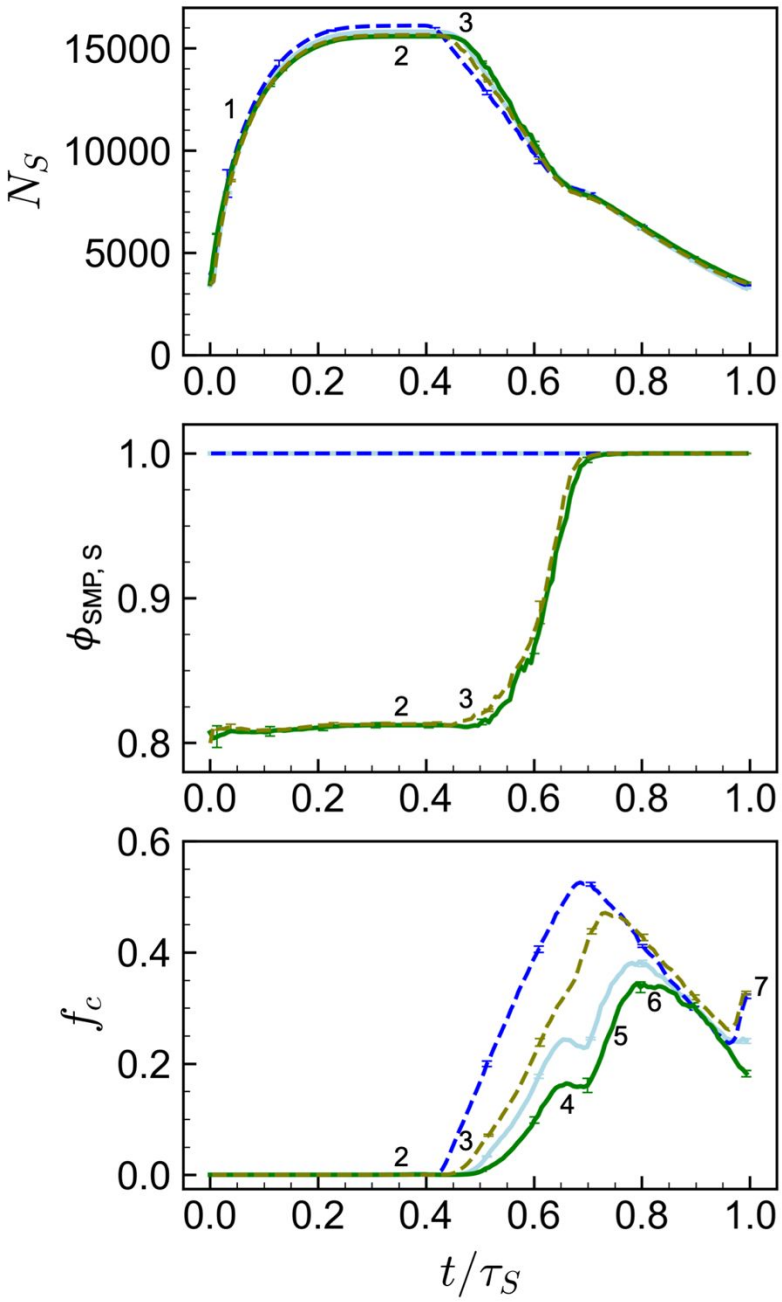

***Figure 4**: Time evolution of the number of particles on the droplet surface (N_S), $\phi_{SMP,\,S}$, and f_c. Dark blue dashed line is a monodisperse D_{SMP} = 220 nm system with $\phi_{SMP,\,B}$ = 1.0, light blue solid line is a D_{SMP} = 220 nm system with 6% particle size dispersity and $\phi_{SMP,\,B}$ = 1.0, light green/olive dashed line is a monodisperse $D_{SP} = D_{SMP}$ = 220 nm system with $\phi_{SMP,\,B}$ = 0.8, and dark green solid line is a $D_{SP} = D_{SMP}$ = 220 nm system with 6% particle size dispersity and $\phi_{SMP,\,B}$ = 0.8. All data shown is for τ_S = 30 s, R_∞ = 3.5 μm, and α = 1.0.*

To demonstrate the localization of particle ordering near the supraball surface, in Figure 5 we plot the fraction of crystalline particles per layer in the outermost six layers of particles (we

describe our strategy for defining a 'layer' in the Methods section) as a function of $\phi_{SMP,\,B}$ for the $D_{SP} = D_{SMP} = 220$ nm case. As $\phi_{SMP,\,B}$ increases, the fraction of crystalline particles per layer also increases, similar to the trends in overall f_c. In general, systems with non-negligible f_c possess a similar degree of ordering in the outer two layers and a significant decrease in ordering in subsequent layers. These results match experimental work by Vogel et al. who found that particle ordering existed primarily near the supraball surface with a disordered region near the center.[18] For the monodisperse $\phi_{SMP,\,B} = 1.0$ system (dashed blue diamonds), we observe ordering that propagates further into the interior of the supraball than the systems with particle size dispersity. We attribute the slight uptick in f_c for the monodisperse systems near $t/\tau_S = 1.0$ seen in Figure 4 above to this additional ordering in the interior layers. This idea is supported by previous computational work by de Nijs et al. on one-component, monodisperse systems in spherical confinement in the limit of low *Pe* that showed crystallinity/ordering that began at the interface and then propagated toward the center of the supraball as η approached the close-packed limit;[53] however, recent work has shown that attractive particle-particle interactions can alter the crystallization mechanism.[62] Overall, the monodisperse systems have higher levels of crystallinity than their polydisperse counterparts regardless of $\phi_{SMP,\,B}$ because the lack of size dispersity likely allows for easier particle incorporation into an ordered structure (ESI Figure S6a).

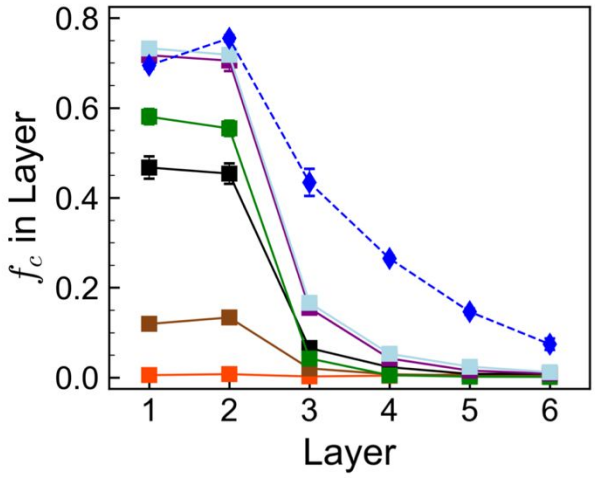

***Figure 5**: Fraction of crystalline particles within the outermost 6 layers in the supraball (1 representing the surface layer). Dark blue diamonds are a monodisperse D_{SMP} = 220 nm system with $\phi_{SMP,\,B}$ = 1.0, light blue squares are a D_{SMP} = 220 nm system with 6% particle size dispersity, purple, green, black, brown, and orange squares are D_{SP} = D_{SMP} = 220 nm systems with 6% particle size dispersity and $\phi_{SMP,\,B}$ = 0.9, 0.8, 0.5, 0.2, and 0.1, respectively. All data shown is for τ_S = 30 s, R_∞ = 3.5 μm, and α = 1.0.*

As τ_S changes from 30 s to 3 s (ESI Figure S6b), the fraction of crystallinity per layer decreases slightly, but the trends remain the same as the τ_S = 30 s results shown in Figure 5. Similarly, changing the particle-interface interactions from strongly attractive to purely repulsive (ESI Figure S7b) decreases the f_c per layer somewhat but does not impact the qualitative trends described above. The f_c per layer for monodisperse systems is more impacted by the interface-particle interaction than for polydisperse systems. Previous work by de Nijs et al. also observed that changing the interface from attractive to repulsive did not have a major impact on the crystallinity observed in the limit of low *Pe*.[53] Experimental work with drying colloidal suspension droplets containing particles experiencing a repulsive interface (in this case water-air) found that the resulting supraballs were still highly ordered, confirming that interface-particle interaction for polydisperse systems does not play a major role in particle ordering.[63]

Discussion:

Before concluding this paper, we include a brief discussion on the potential impact of our chosen simulation methodology on our results. There are two key physical phenomena that our implicit solvent Langevin dynamics method necessarily cannot capture: 1) hydrodynamic effects resulting from the flow of solvent molecules during the emulsion assembly and 2) the soft, deformable nature of the real liquid-liquid interface. The true impact of these phenomena can only be definitively explored with an explicit solvent approach; however even with the latest hardware, accessing the experimentally relevant length and timescales probed in this work would be prohibitively computationally expensive with explicit solvents. For example, an explicit solvent approach with the solvent represented as a CG bead with a 1 nm diameter would require up to $\sim 10^{13}$ solvent particles just to solvate the inside of the emulsion droplet. Furthermore, to explicitly model the liquid-liquid interface in the emulsion assembly process, additional solvent of a different chemistry would be required to surround the solvent molecules within the emulsion droplet; this would further increase the number of solvent particles required. Therefore, such an explicit solvent approach would need to handle size scales ranging from ~1 nm (solvent) to hundreds of nm (nanoparticles) to tens of microns (emulsion droplet), which is not feasible with any of the current computational techniques. Thus, to understand the potential implications of our chosen implicit solvent approach, we review the available literature on the explicit effects from solvent (e.g., hydrodynamics) in analogous systems.

One area where there has been progress in elucidating hydrodynamic effects is in *evaporative* assembly (in contrast to emulsion assembly which is the focus of this paper), albeit with some conflicting conclusions. Several studies focused on evaporative assembly suggest that neglecting hydrodynamics can strongly affect the regimes of particle concentration, size ratio, and

Pe where auto-stratification is observed in drying films.[29, 40, 64] However, Tang et al. performed implicit and explicit solvent simulations of drying binary colloidal films, and in seeming conflict with other recent work, they found that both approaches produced comparable structures.[32] To date, the body of work that demonstrated a significant hydrodynamic effect focused on either polymer-polymer mixtures[64] or polymer-colloid mixtures with drastically different size scales for the two solutes,[29] while the system explored in Tang et al.[32] contains particles with less extreme size disparities. The variability in particle size-scales or some subtle difference between particle and polymer systems could be responsible for the conflicting results. Howard et al. investigated solvent effects in the evaporative film assembly of single-component colloidal crystals, and found that at high-*Pe*, the dynamics and mechanistic pathways of assembly were different between implicit and explicit solvent simulations but the final crystalline structures appeared similar.[34] And in the context of spherical confinement, a recent study on evaporative colloidal assembly in spherical droplets found that implicit solvent simulations *qualitatively* agreed with experimental results, though the authors noted *quantitative* differences that they attribute to hydrodynamic effects and/or differences in droplet size scales between simulations and experiments.[39]

In light of the available literature in evaporative assembly, we believe that neglecting hydrodynamics may have a minor *quantitative* impact on our results but will not impact the *qualitative* trends or the key steps in the assembly pathway. Due to the fundamental differences between the assembly mechanism probed herein (driven by strongly attractive particle-interface interactions) and diffusiophoresis-based auto-stratification, we expect our results to be less sensitive to the treatment of hydrodynamic effects than the systems reviewed above. In contrast to a diffusiophoretic process, where surface segregation is a result of a careful balance of particle transport and interfacial motion throughout the course of the assembly process (often occurring at

Pe significantly higher than probed in this work), in our system, particle transport only plays a role in the very earliest stages of assembly when particles are diffusing and adsorbing to the liquid-liquid interface. As seen from Figure 4, the most significant changes in surface composition and ordering all occur well after the formation of a jammed surface layer, where diffusive particle transport is negligible. Changes in particle motion during the early stages of assembly may affect the initial composition of the jammed surface layer, which could then propagate to change the final supraball surface composition. However, we expect this impact to be small due to the relatively low *Pe*, low particle concentration, moderate particle size ratio, and large droplet/particle size ratio during the initial stages of the assembly process. Furthermore, our prior work using the same implicit solvent simulation model and methodology demonstrated qualitative agreement with experimental trends as a function of particle size.[21] We note that there have been some important methodological advances to incorporate hydrodynamics into analogous systems.[35, 65-67] For example, recent Stokesian dynamics simulations explored equilibrium diffusion of a hydrodynamically interacting suspension in spherical confinement; they discovered that radial diffusion near the droplet surface decreased compared to unconfined diffusion, and this decrease was dependent on the particle concentration and size ratio of particles to the confined volume.[65] Adapting these schemes to the binary systems and/or to the shrinking spherical geometry probed herein is a promising future avenue of study that could help shed light on the impact of hydrodynamics in this system, however it will necessitate some compromise in particle sizes and simulation system sizes explored. Another potential option would be to apply the dissipative particle dynamics (DPD) thermostat as an alternative to the Langevin thermostat used in this work, which would incorporate hydrodynamic effects at an approximate level through the pairwise dissipative and random forces.[68-70]

Conclusions:

In this work, we map the rich physics underlying the structures formed in the emulsion assembly of binary nanoparticle mixtures into spherical supraballs as a function of a large design space comprised of nanoparticle size, chemistry, mixture composition, assembly time, and emulsion droplet size. We focus on the regime of strongly attractive particle-interface interactions, where one particle type (SMP) extends further into the oil (majority) phase than the other (SP), with assembly occurring at moderate *Pe* ($0.6 < Pe < 30$). We show how the surface and interior composition of the supraball (important for coloration in optical applications) can be tuned by adjusting particle size, particle mixture composition, and supraball size. More complex arrangements such as core-shell supraballs can also be produced in the limit of small supraballs. We also discuss the phenomena that control particle ordering (i.e., iridescence) in these materials. Ordering only occurs in systems with symmetric particle sizes, largely near the supraball surface. A finite assembly time, particle size dispersity, and the curvature of the supraball surface all serve to suppress ordering, and we discuss regimes where ordering is and is not prevalent. We also present a detailed view of the key steps in the assembly process to understand how the development of surface structure and composition occurs over time. We envision that these results (focusing on particle localization/structure within the supraballs) could be subsequently combined with theoretical methods to calculate optical properties as a function of known spatial variations in refractive index (such as obtaining reflectance spectra via finite-difference time-domain (FDTD) simulations[17, 71]); such an approach would explicitly link the supraball assembly design space to structural color response. As such, this work provides design rules for the development of structurally-colored optical materials and also extrapolates more generally to the assembly of

binary particle mixtures in shrinking spherical confinement, with relevance to other important processes such as spray drying and porous materials fabrication.

Conflicts of Interest:

The authors declare no conflicts of interest.

Acknowledgements:

T.E.G., C.M.H., and A.J. acknowledge financial support from the Air Force Office of Scientific Research (MURI-FA 9550-18-1-0142). This work was supported by the use of computational resources from the University of Delaware (Farber and Caviness clusters) and the Extreme Science and Engineering Discovery Environment (XSEDE) Stampede cluster (allocation MCB100140), which is supported by NSF grant ACI-1548562.

References:

1. M. Grzelczak, J. Vermant, E. M. Furst and L. M. Liz-Marzan, *ACS Nano*, 2010, **4**, 3591-3605.
2. R. McGorty, J. Fung, D. Kaz and V. N. Manoharan, *Mater. Today*, 2010, **13**, 34-42.
3. A. Boker, J. He, T. Emrick and T. P. Russell, *Soft Matter*, 2007, **3**, 1231-1248.
4. F. Bresme and M. Oettel, *J. Phys.: Condens. Matter*, 2007, **19**, 413101.
5. P. Pieranski, *Phys. Rev. Lett.*, 1980, **45**, 569-572.
6. B. J. Park and E. M. Furst, *Soft Matter*, 2010, **6**, 485-488.
7. M. A. Boles, M. Engel and D. V. Talapin, *Chem. Rev.*, 2016, **116**, 11220-11289.
8. Y. Lin, H. Skaff, T. Emrick, A. D. Dinsmore and T. P. Russell, *Science*, 2003, **299**, 226-229.
9. V. N. Manoharan, M. T. Elsesser and D. J. Pine, *Science*, 2003, **301**, 483-487.

10. Y. S. Cho, G. R. Yi, J. M. Lim, S. H. Kim, V. N. Manoharan, D. J. Pine and S. M. Yang, *J. Am. Chem. Soc.*, 2005, **127**, 15968-15975.

11. A. Fortini, I. Martin-Fabiani, J. L. De La Haye, P. Y. Dugas, M. Lansalot, F. D'Agosto, E. Bourgeat-Lami, J. L. Keddie and R. P. Sear, *Phys. Rev. Lett.*, 2016, **116**, 118301.

12. F. Bai, D. S. Wang, Z. Y. Huo, W. Chen, L. P. Liu, X. Liang, C. Chen, X. Wang, Q. Peng and Y. D. Li, *Angew. Chem. Int. Ed.*, 2007, **46**, 6650-6653.

13. V. N. Manoharan, *Science*, 2015, **349**, 1253751.

14. C. Zhu, W. Y. Xu, L. S. Chen, W. D. Zhang, H. Xu and Z. Z. Gu, *Adv. Funct. Mater.*, 2011, **21**, 2043-2048.

15. Y. J. Zhao, L. R. Shang, Y. Cheng and Z. Z. Gu, *Acc. Chem. Res.*, 2014, **47**, 3632-3642.

16. J. C. Cui, W. Zhu, N. Gao, J. Li, H. W. Yang, Y. Jiang, P. Seidel, B. J. Ravoo and G. T. Li, *Angew. Chem. Int. Ed.*, 2014, **53**, 3844-3848.

17. M. Xiao, Z. Y. Hu, Z. Wang, Y. W. Li, A. D. Tormo, N. Le Thomas, B. Wang, N. C. Gianneschi, M. D. Shawkey and A. Dhinojwala, *Sci. Adv.*, 2017, **3**, e1701151.

18. N. Vogel, S. Utech, G. T. England, T. Shirman, K. R. Phillips, N. Koay, I. B. Burgess, M. Kolle, D. A. Weitz and J. Aizenberg, *Proc. Natl. Acad. Sci. U.S.A.*, 2015, **112**, 10845-10850.

19. Y. J. Zhao, Z. Y. Xie, H. C. Gu, C. Zhu and Z. Z. Gu, *Chem. Soc. Rev.*, 2012, **41**, 3297-3317.

20. L. D'Alba and M. D. Shawkey, *Physiol. Rev.*, 2019, **99**, 1-19.

21. M. Xiao, Z. Hu, T. E. Gartner, III, X. Yang, W. Li, A. Jayaraman, N. C. Gianneschi, M. D. Shawkey and A. Dhinojwala, *Sci. Adv.*, 2019, **5**, eeax1254.

22. M. P. Howard, A. Nikoubashman and A. Z. Panagiotopoulos, *Langmuir*, 2017, **33**, 3685-3693.

23. Y. F. Tang, G. S. Grest and S. F. Cheng, *Langmuir*, 2018, **34**, 7161-7170.

24. R. P. Sear, *J. Chem. Phys.*, 2018, **148**, 134909

25. A. F. Routh, *Rep. Prog. Phys.*, 2013, **76**, 046603.

26. A. K. Atmuri, S. R. Bhatia and A. F. Routh, *Langmuir*, 2012, **28**, 2652-2658.

27. I. Martin-Fabiani, A. Fortini, J. L. de la Haye, M. L. Koh, S. E. Taylor, E. Bourgeat-Lami, M. Lansalot, F. D'Agosto, R. P. Sear and J. L. Keddie, *ACS Appl. Mater. Interfaces*, 2016, **8**, 34755-34761.

28. A. Fortini and R. P. Sear, *Langmuir*, 2017, **33**, 4796-4805.

29. R. P. Sear and P. B. Warren, *Phys. Rev. E*, 2017, **96**, 062602.

30. T. P. Bigioni, X. M. Lin, T. T. Nguyen, E. I. Corwin, T. A. Witten and H. M. Jaeger, *Nat. Mater.*, 2006, **5**, 265-270.

31. S. F. Cheng and G. S. Grest, *J. Chem. Phys.*, 2013, **138**, 064701.

32. Y. F. Tang, G. S. Grest and S. F. Cheng, *J. Chem. Phys.*, 2019, **150**, 224901.

33. M. P. Howard, A. Nikoubashman and A. Z. Panagiotopoulos, *Langmuir*, 2017, **33**, 11390-11398.

34. M. P. Howard, W. F. Reinhart, T. Sanyal, M. S. Shell, A. Nikoubashman and A. Z. Panagiotopoulos, *J. Chem. Phys.*, 2018, **149**, 094901.

35. M. Wang and J. F. Brady, *Soft Matter*, 2017, **13**, 8156-8170.

36. D. K. Makepeace, A. Fortini, A. Markov, P. Locatelli, C. Lindsay, S. Moorhouse, R. Lind, R. P. Sear and J. L. Keddie, *Soft Matter*, 2017, **13**, 6969-6980.

37. J. J. Zhou, Y. Jiang and M. S. Doi, *Phys. Rev. Lett.*, 2017, **118**, 108002.

38. M. Schulz and J. L. Keddie, *Soft Matter*, 2018, **14**, 6181-6197.

39. W. Liu, J. Midya, M. Kappl, H. J. Butt and A. Nikoubashman, *ACS Nano*, 2019, **13**, 4972-4979.

40. J. F. Brady, *J. Fluid Mech.*, 2011, **667**, 216-259.

41. M. Xiao, A. Dhinojwala and M. Shawkey, *Opt. Express*, 2014, **22**, 14625-14636.

42. R. Everaers and M. R. Ejtehadi, *Phys. Rev. E*, 2003, **67**, 041710.

43. T. Young, *Philos. Trans. R. Soc. London*, 1805, **95**, 65-87.

44. S. Plimpton, *J. Comput. Phys.*, 1995, **117**, 1-19.

45. A. R. Leach, *Molecular Modelling: Principles and Applications*, Pearson Education, Essex, 2nd edn., 2001.

46. T. Watanabe, C. G. Lopez, J. F. Douglas, T. Ono and J. T. Cabral, *Langmuir*, 2014, **30**, 2470-2479.

47. C. E. Udoh, V. Garbin and J. T. Cabral, *Langmuir*, 2016, **32**, 8131-8140.

48. C. E. Udoh, J. T. Cabral and V. Garbin, *Sci. Adv.*, 2017, **3**, eaao3353.

49. W. N. Sharratt, A. Brooker, E. S. J. Robles and J. T. Cabral, *Soft Matter*, 2018, **14**, 4453-4463.

50. F. Aurenhammer, *ACM Comput. Surv.*, 1991, **23**, 345-405.

51. C. B. Barber, D. P. Dobkin and H. Huhdanpaa, *ACM T. Math. Software*, 1996, **22**, 469-483.

52. P. J. Steinhardt, D. R. Nelson and M. Ronchetti, *Phys. Rev. B*, 1983, **28**, 784-805.

53. B. de Nijs, S. Dussi, F. Smallenburg, J. D. Meeldijk, D. J. Groenendijk, L. Filion, A. Imhof, A. van Blaaderen and M. Dijkstra, *Nat. Mater.*, 2015, **14**, 56-60.

54. W. Humphrey, A. Dalke and K. Schulten, *J. Mol. Graphics Modell.*, 1996, **14**, 33-38.

55. A. Kawamura, M. Kohri, S. Yoshioka, T. Taniguchi and K. Kishikawa, *Langmuir*, 2017, **33**, 3824-3830.

56. M. D. Shawkey, L. D'Alba, M. Xiao, M. Schutte and R. Buchholz, *J. Morphol.*, 2015, **276**, 378-384.

57. Y. S. Cho, S. H. Kim, G. R. Yi and S. M. Yang, *Colloid Surf. A*, 2009, **345**, 237-245.

58. W. Sun, S. L. Chen, H. L. Zhu, M. R. Xu and A. J. Wang, *J. Colloid Interface Sci.*, 2017, **502**, 219-226.

59. D. Wang, M. Hermes, R. Kotni, Y. T. Wu, N. Tasios, Y. Liu, B. de Nijs, E. B. van der Wee, C. B. Murray, M. Dijkstra and A. van Blaaderen, *Nat. Commun.*, 2018, **9**, 2228.

60. A. M. Mascioli, C. J. Burke, M. Q. Giso and T. J. Atherton, *Soft Matter*, 2017, **13**, 7090-7097.

61. C. J. Burke and T. J. Atherton, **arXiv:1605.09478v2 [cond-mat. soft]**.

62. F. Montanarella, J. J. Geuchies, T. Dasgupta, P. T. Prins, C. van Overbeek, R. Dattani, P. Baesjou, M. Dijkstra, A. V. Petukhov, A. van Blaaderen and D. Vanmaekelbergh, *Nano Lett.*, 2018, **18**, 3675-3681.

63. M. Wozniak, G. Derkachov, K. Kolwas, J. Archer, T. Wojciechowski, D. Jakubczyk and M. Kolwas, *Langmuir*, 2015, **31**, 7860-7868.

64. A. Statt, M. P. Howard and A. Z. Panagiotopoulos, *J. Chem. Phys.*, 2018, **149**, 024902.

65. C. Aponte-Rivera, Y. Su and R. N. Zia, *J. Fluid Mech.*, 2018, **836**, 413-450.

66. M. P. Howard, A. Z. Panagiotopoulos and A. Nikoubashman, *Comput. Phys. Commun.*, 2018, **230**, 10-20.

67. M. P. Howard, A. Nikoubashman and J. C. Palmer, *Curr. Opin. Chem. Eng.*, 2019, **23**, 34-43.

68. P. Espanol and P. B. Warren, *J. Chem. Phys.*, 2017, **146**, 150901.

69. T. Soddemann, B. Dunweg and K. Kremer, *Phys. Rev. E*, 2003, **68**, 046702.

70. C. Pastorino, T. Kreer, M. Muller and K. Binder, *Phys. Rev. E*, 2007, **76**, 026706.

71. H. Galinski, G. Favraud, H. Dong, J. S. T. Gongora, G. Favaro, M. Dobeli, R. Spolenak, A. Fratalocchi and F. Capasso, *Light Sci. Appl.*, 2017, **6**, e16233.